Lawrence Radiation Laboratory

UNIVERSITY OF CALIFORNIA

LIVERMORE

UCRL-50901

DYNAMIC YIELD STRENGTHS

OF LIGHT ARMOR MATERIALS

W. H. Gust

E. B. Royce

Contents

DYNAMIC YIELD STRENGTHS
OF LIGHT ARMOR MATERIALS

Abstract

Inclined mirrors and prisms have been used to determine Hugoniot elastic limits (HEL's) for the light ceramics B_4C, BeO, four grades of Al_2O_3, SiC, TiB_2, AlB_{12}, $TiBe_{12}$, Be_2B, and $ZrBe_{13}$; $\langle 100 \rangle$, $\langle 110 \rangle$, and $\langle 111 \rangle$ Si; and a maraging steel, Vascomax 350. Hugoniot parameters to about 1 Mbar were measured for B_4C, BeO, and the four aluminas, and to about 0.5 Mbar for Si. Four-wave shock structures were observed for $\langle 110 \rangle$ and $\langle 111 \rangle$ Si. These have been related to the HEL's and to two successive phase transitions. In Vascomax 350, a three-wave structure was seen which appears to be related to the 130-kbar transition in Fe. Three-wave structures were also observed in $\langle 100 \rangle$ Si and AlB_{12}.

Introduction

The study of the physical phenomena associated with ballistic penetration has been aided by a series of measurements of the dynamic compressive yield strengths or Hugoniot elastic limits (HEL's) for a number of high-strength materials, particularly ceramics.[*] Knowledge of the dynamic response of potential armor materials to shock loading was the primary objective, but since there was a dearth of information concerning response of armor ceramics in the deformational regime, the measurements were, in some instances, extended to higher pressure levels — on the order of 1 Mbar. Material response was observed as driving pressure and shock propagation distance were varied, and the dependence of shock propagation characteristics on porosity and impurity content were noted. Of more fundamental interest,

the response of single crystals to shock loading along different axes was recorded.

A Hugoniot elastic limit is measured through the resolution of the two-wave shock structure which is usually formed

-1-

by the elastic and the more slowly propagating deformational wave. Widespread application of the techniques involved is relatively new; well over half of the existing data on Hugoniot elastic limits is less than five years old.

The hydrostatic compression of Al_2O_3 has been measured by Bridgman[1] and by Hart and Drickamer,[2] and the hydrostatic compression of BeO by Weir and Shastis[3] and Cline and Stephens.[4] Sonic velocities have been measured under hydrostatic pressure on Al_2O_3[5-7] and on BeO.[8] Single-shock compression data at high pressures have been reported for Al_2O_3 by McQueen and Marsh,[9] and similar work by Hord on BeO has been reported by Cline and Stephens.[4] Two-wave measurements on Al_2O_3 have been made by Brook and Graham[10] and by Ahrens, Gust, and Royce.[11]

Hydrostatic high-pressure measurements of the resistivity of crystalline silicon have been reported by Minomura and Drickamer[12] and x-ray diffraction experiments at high pressure were reported by Wentorf and Kasper[13] and by Jamieson.[14] McQueen[15] reported measurements of the Hugoniot elastic limit for Si made by Wackerle, while Al' tshuler[16] and Pavlovskii[17] reported similar results.

Here we report information[18] on the Hugoniot elastic limits, shock compression parameters, and elastic properties for polycrystalline forms of B_4C, BeO, four grades of Al_2O_3, SiC, TiB_2, AlB_{12}, $TiBe_{12}$, Be_2B, and $ZrBe_{13}$. Results from shocks propagated along the $\langle 100 \rangle$, $\langle 110 \rangle$, and $\langle 111 \rangle$ axes of crystalline silicon and the compressional characteristics of a maraging steel are also recorded.

Procedure

Explosive systems were used to generate shocks which resulted in ceramic pressures ranging from about 180 to 1000 kbar for this series of experiments. Data at pressures greater than 500 kbar were obtained through the use of the flash-gap technique.[19] Experiments at pressures below 500 kbar were done with either inclined mirrors[20] or inclined prisms,[21] the latter being the more sensitive of the two techniques.

The geometry used in the inclined mirror experiments is shown in Fig. 1. It has the advantage of simultaneously providing continuous direct measurement of the free-surface velocity of the base plate and of the two samples as well as shock

velocity through the two samples. For most experiments, two mirrors were used to obtain the state of the base plate, which was of 2024 aluminum, while the other two provided separate measurements on two samples of material. In most experiments, the two samples were of identical material. The angles of inclination were 3° or 5° for the base-plate mirrors, and 1.5° and 3° for the mirrors on the samples.

The mirrors are intensely illuminated with a high-explosive-driven argon light source, and the reflected image is viewed with a rotating-mirror streaking camera, as shown schematically in Fig. 1. The initial shock causes the free surface to move across the wedge-shaped gap at

From mirror on base plate

From mirror on sample

Rotating mirror

A

Relay system

Field lens

Section A-A

0.001 in. slit

Film surface

A

48-in. achromat

Sample

Turning mirror

Plane-wave generator

HE

Argon-filled, high explosive light source

Base plate (rotated 90°)

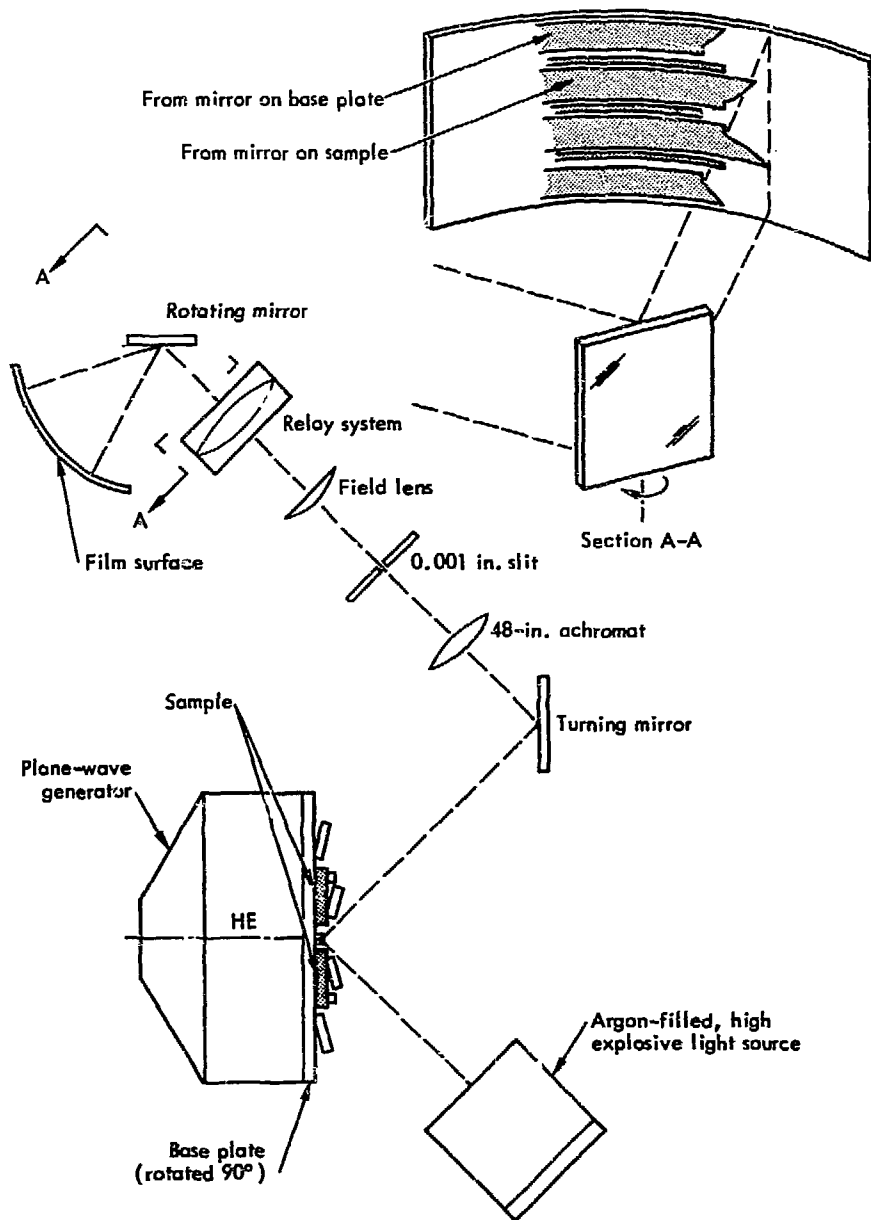Fig. 1. Experimental geometry for inclined-mirror experiments. The inclined mirrors are silvered on the side next to the samples, are illuminated with an explosively driven argon light source, and are viewed through a small slit in a rotating-mirror streaking camera.

velocity U_{fs_1}, where it progressively contacts the mirror surface along the in- clined length. Reflection along the mir- ror is then progressively destroyed by

the moving impact point so that the light is progressively cut off. The velocity of the light-dark discontinuity is proportional to the material free-surface velocity, and, when viewed through a small slit, the discontinuity is recorded as a slope on the streaking camera record. A subsequent wave moving with velocity $U_{s_2} + U_{p_1}$ (where U_s is the shock velocity and U_p the particle velocity) overtakes the boundary moving at U_{fs_1} and a different, faster contact rate occurs; this rate results in a different slope, which is related to U_{fs_2}, the velocity at which the free surface now moves. A similar procedure may be applied to any additional waves.

An experimental record and the preshot mirror array are shown in Fig. 2. The traces show examples of the film cut-off angles which are related to loss of reflectivity caused by the elastic and deformational waves. The Hugoniot parameters are related to the records through the relations

$$U_{s_1} = \frac{x_1 - x_0}{t_1 - t_0} = \frac{HW}{Z_1} \qquad (1)$$

and

$$U_{fs_1} = \frac{W \tan \alpha}{M \tan \gamma} , \qquad (2)$$

where H is the sample thickness, Z_1 the flat mirror cut-off position on the film record, W the camera streaking rate, M the magnification factor which relates the film record to actual experiment dimensions, α the angle of mirror inclination, and γ the angle between the free surface film trace and the normal to the camera sweep, as shown in Fig. 1. Small corrections are applied to account for deviations from ideal geometry.

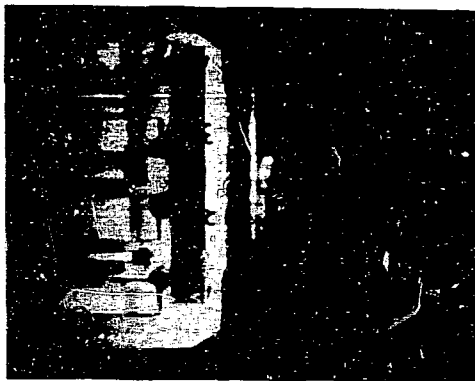In these experiments the particle velocity associated with the elastic shock was

Fig. 2. Typical record from an inclined-mirror experiment on B_4C ceramic at 430 kbar. At the left is a setup picture of the experiment, taken with the camera slit removed. For the shot record, time progresses from left to right, the important part of the record being the light cutoff at the right-hand side.

obtained from the free-surface approximation, $U_{p_1} = U_{fs_1}/2$. This implies that the entropy increase related to the elastic shock state is small, and that material properties in the initial and elastic shock states are substantially the same. The shock stress and volume corresponding to the elastic limit are then obtained through use of the Hugoniot conservation relations (in laboratory coordinates), namely,

$$\sigma_1 = \rho_0 U_{s_1} U_{p_1},$$

and

$$(V_1/V_0) = 1 - \left(U_{p_1}/U_{s_1}\right).$$

Figure 3 displays an x-versus-t representation of the wave reflections which result from the interaction of the elastic wave with the free surface. It has been found that U_{s_2} is relatively insensitive to the values used for U'_{s_1} and U'_{s_2}, and it may be assumed that the shock and rarefaction

processes for the elastic wave are nearly reversible. Hence, good approximations are $U'_{s1} = U_{s1} - U_{p1}$ and $U'_{s2} = U_{s1} + U_{fs_1}$. The apparent second shock velocity is given by

$$U_{s_2} = \frac{x_2 - x_0}{t_2 - t_0}$$

$$= \frac{x_1 - x_0 + (t_2 - t_1)U_{fs_1}}{t_2 - t_0}$$

$$= \frac{H + U_{fs_1}(t_2 - t_1)}{t_2 - t_0}. \tag{3}$$

It may then be shown[11] that the true second shock velocity is given by

$$U_{s_2} = \frac{U'_{s_1}\overline{U}_{s_2}\left(U_{s_1} - U_{fs_1}\right) + U_{s_1}U'_{s_2}\left(\overline{U}_{s_2} - U_{fs_1}\right) - U'_{s_1}U'_{s_2}\left(U_{s_1} - \overline{U}_{s_2}\right)}{U'_{s_2}\left(U_{s_1} - U_{fs_1}\right) + U'_{s_1}\left(\overline{U}_{s_2} - U_{fs_1}\right) - U_{fs_1}\left(U_{s_1} - \overline{U}_{s_2}\right)}. \tag{4}$$

The final stress for a two-wave shock is obtained from

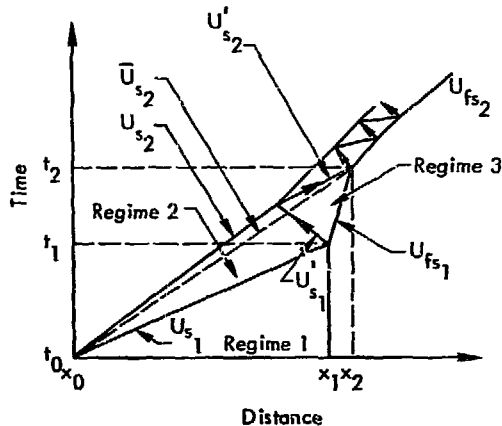$$\sigma_2 = \sigma_1 + \rho_1\left(U_{s_2} - U_{p_1}\right)\left(U_{p_2} - U_{p_1}\right),$$

Fig. 3. Schematic representation of two waves in the ceramic sample and their interaction with the free surface.

where

$$\rho_1 = \rho_0\left(\frac{U_{s_1}}{U_{s_1} - U_{p_1}}\right). \tag{5}$$

When two-wave shock structures were measured, the deformational particle velocity, U_{p_2}, was determined by the impedance matching technique.[22] For this technique, the state of the aluminum base plate was determined from free-surface velocity measurements made during each experiment. Particle velocity was also determined by use of the free-surface velocity approximation, $U_{p_2} = U_{fs_2}/2$. Precisions of the shock and particle velocity measurements for the deformational shock front are usually better than ±1% and ±3%, respectively. Uncertainty in the determination of particle velocity for the elastic shock is usually about 5%, although in a few experiments the mirrors were not in contact with the samples and the resulting gap caused gross error in the measurement for the elastic wave. In some instances the recorded film trace cutoff was curved, and the cutoff angle was taken to be the initial slope of the curve.

The inclined prism technique is similar to the inclined mirror technique in application. The difference is that reflection from the mirrors is from a metallized surface, while the prisms operate on total internal reflection, associated with the difference in the indexes of refraction of the glass and vacuum. The loss of reflectivity of the mirrors is caused by the destruction of the reflecting surface on impact, while

for the prisms the loss of reflectivity is caused by a drastic change of the index of refraction of the medium outside the prism as the sample free surface moves into full contact. As the shot is set up, the prism contacts the sample surface at only a few points.

Materials subject to shock-induced phase transitions may exhibit shock structures with more than two waves. In this instance, the elastic wave is identified by the equivalence of U_{S_1} with C_L, the ultrasonically determined longitudinal sound speed at 1 bar, and any remaining waves are related to either phase transitions or the final state achieved in the particular experiment. In experiments on Vascomax 350, three-wave shock structures were observed. Shocks that propagated along the $\langle 110 \rangle$ and $\langle 111 \rangle$ axes of the crystalline silicon exhibited four-wave structures. A detailed analysis of the interactions of a three- or four-wave shock structure is beyond the scope of this report; hence, no corrections are made on velocities of second, third, or fourth shocks. In other words, the data reduction procedure uses apparent or average values for the shock velocities. The more complex waves are

then evaluated through an extension of the equations,

$$U_{s_n} = \frac{H + \sum_1^n U_{rs_{n-1}} (t_n - t_{n-1})}{t_n - t_0} ,$$

$$U_{fs_n} = \frac{W \tan \alpha}{M \tan \gamma_n} ,$$

$$U_{p_n} = \frac{U_{fs_n}}{2} . \qquad (6)$$

Here Z (Eq. (1)) is either the flat mirror cutoff position on the film record or the point of intersection of the extrapolation for each of the successive free-surface velocity slopes.

Application of the conservation of mass and momentum across the shock front leads to the Hugoniot equations which, for multiple wave structures, may be expressed in terms of stress and volume as

$$\sigma_n = V_{n-1}^{-1} \left(U_{s_n} - U_{p_{n-1}} \right) \left(U_{p_n} - U_{p_{n-1}} \right)$$
$$+ \sigma_{n-1} \qquad (7)$$

$$V_n = V_{n-1} \left(U_{s_n} - U_{p_n} \right) \Big/ \left(U_{s_n} - U_{p_{n-1}} \right) \qquad (8)$$

Materials

The hot-pressed polycrystalline B_4C was fabricated by the Norton Company of Worcester, Massachusetts.[*] Chemical and spectrochemical analyses supplied by

[*] Reference to a company or product name does not imply approval or recommendation of the product by the University of California or the U.S. Atomic Energy Commission to the exclusion of others that may be suitable.

the manufacturer showed a B-to-C ratio of 3.93:1 and B + C = 98.12%. The major impurities are listed in Table 1. The structure is rhombohedral with a = 5.63 Å, c = 12.14 Å.[23] Theoretical density of the conglomerate was about 2.52 g/cc; actual density was about 2.50 g/cc.

The BeO studied was a commercially available polycrystalline material,

Table 1. Impurities in ceramics studied (in wt%).

Impurity	B_4C	BeO	Al_2O_3 AD-85	Al_2O_3 P-3142-1	Al_2O_3 Al-995	Al_2O_3 Hot pressed
B						<0.02
Si		0.22	7.0		0.2	0.3
as SiO_2	0.08	0.46	15.0	~2.0	0.4	0.6
Ca			1.5		0.03	0.02
as CaO	0.1		2.1	~0.5	0.04	0.03
Mg		0.09	2.0		0.3	0.2
as MgO	0.02	0.16	3.3	~0.5	0.5	0.3
Ba			0.8			
as BaO			0.9			
Fe		0.01	0.3	0.02	0.07	0.03
as Fe_2O_3		0.014	0.4	0.03	0.1	0.04
V						
as V_2O_3					0.01	
Ti			0.2		0.01	
as TiO_2			0.3		0.015	
Ni						
as NiO	0.01-0.05					
Cr				0.5		
as Cr_2O_3				0.8		
Na		0.01	0.05			0.3
as Na_2O		0.02	0.07			0.4
Ga						0.02
Al_2O_3	0.1-0.5					
Source	Mfr.	Mfr.	LRL	LRL	LRL	Mfr.

designated as Thermalox-995 by Brush Beryllium Company, Elmira, Ohio. This ceramic has a nominal BeO content of 99.5%. Major impurities are listed in Table 1. The structure of crystalline BeO is the hexagonal wurtzite structure with a = 2.70 Å, c = 4.40 Å. Theoretical density of the material was about 3.01 g/cc; actual density was 2.84 g/cc.

Four grades of alumina, which varied considerably in porosity and impurity content, were studied. These included Coors AD-85 manufactured by Coors Porcelain Company, Golden, Colorado; Diamonite P-3142-1 from Diamonite Products Company, Shreve, Ohio; a high-purity grade fabricated by a hot-pressing technique by the Carborundum Company, Niagra Falls, New York; and data taken from Ref. 11 for Wesgo-995, produced by the Western Gold and Platinum Company, Belmont, California. Table 1 lists impurities present in amounts greater than 0.01%. Alumina is hexagonal, with a = 4.758 Å, c = 12.925 Å.[23]

-7-

Table 2. Hugoniot parameters.

	B₄C	BeO	Al₂O₃ Hot pressed	Al-995	P-3142-1	AD-85	SiC	TiB₂	AlB₁₂	TiBe₁₂	be₂B	ZrBe₁₃	Silicon (100)	(110)	(111)	Vascomax 350	
Density, ρ_0 (g/cm³)	2.50	2.84	3.92	3.81	3.72	3.42	3.09	4.516	2.54	2.284	1.99	2.728	2.330			8.08	
Theo density (g/cm³)	2.52[b]	3.01[a]	3.96[a]	3.97[a]	3.94[a]	3.66[a]	2.9-3.0[b]	4.63[b]	2.6-2.7[b]	2.28[b]	2.4[b]	2.726[b]					
Void fraction	0.020	0.056	0.008	0.040	0.055	0.066		~0.02	~0.02-0.06	~0	~0.17	0					
Ultrasonic moduli[c] (Mbar)																	
Longitudinal, L	4.75	3.78	4.40	4.07	3.71	2.67	3.88	5.72	3.57	3.04	2.88	2.04	1.67	1.98	2.04	2.71	
Shear, G	1.82	1.42	1.49	1.47	1.29	0.88	1.64	2.34	1.63	1.27	1.24	1.20	0.80	{0.76 / 0.50}	0.61	0.76	
Bulk, B[d]	2.32	1.88	2.40	2.11	1.99	1.50	1.70	2.59	1.39	1.34	1.23	1.22	1.00ⁿ			1.72	
Hugoniot elastic limit (kbar)																	
σ_{HEL}[g]	154	82	134	83	88	61	83	81	32[e]	54[e]	65[e]	71[e]	92	53	54	48	
$\Delta\sigma = \frac{2}{3}Y_0 \left(\frac{L-B}{L}\right)\sigma_{HEL}$[f]	79	41	62	40	41	27	47	44	25[b]	30[e]	37[e]	42[e]	38	20	28	78	
Hugoniot fit																	
A_1[h] (Mbar)	1.8	0.75	2.25	1.4	0.5	0	1.6 1.35[j]	2.45	1.7[e,l]	1.55[e]	1.1[e]	1.2[e]	1.13[p]	1.15[p,q]		1.8[m]	0.65[m]
A_2[h] (Mbar)	3.2	4.0	5.0	5.7	7.8	4.7	0 0[j]	12.4	0[e,l]	0[e]	0[e]	0[e]	-2.0[p]	-2.0[p,q]		0[m]	6.2[m]
P_{min}[i] or P_{meas}[k] (Mbar)	0.2	0.15	0.2	0.2	0.2	0.15	0.1 0.25[j]	0.14	~0.1[e]	0.2[e]	~0.1[e]	~0.2[b]	0.05[p]	0.05[f,q]			0.14[m]
P_{max}[i] (Mbar)	1.0	0.9	1.2	1.2	1.0	1.0	0.4 1.0[j]	0.45		~0.2[b]		~0.2[e]	0.2[p]	0.7[p,q]		0.14[m]	0.6[m]

[a] Impurities included.

[b] Impurities not included.

[c] Measured by H. L. Dunegan and P. L. Knauss.

[d] B = L - 4G/3.

[e] Only two shots fired.

[f] Ultrasonic values of L and B used.

[g] Measured on 6-mm samples.

[h] $P = \sigma_{Hug} - \Delta\sigma = A_1\mu + A_2\mu^2 + A_3\mu^3$, $\mu = (V_0 - V)/V$. (Normally $A_3 = 0$.)

[i] P_{min} and P_{max} define range of data and validity of the fit.

[j] $A_3 = 8$ Mbar.

[k] P_{meas} indicates the general pressure region where measurements were made.

[l] Ignores phase transition at 62 kbar; multiple-wave structure was observed.

[m] Phase transitions at 160 kbar; multiple-wave structure for 0.10 < P < 0.34.

[n] Best values of elastic moduli appear to be $C_{11} = 1.67$, $C_{12} = 0.67$, $C_{44} = 0.70$.

[p] Ignores phase transitions given in Table 4. Multiple-wave structures were observed; fit applies to all orientations.

[q] $A_3 = 2.8$ Mbar.

Impurity analyses for the other materials listed in Table 2 were not available. Starting powders of the highest purity obtainable were stated to have been used in their manufacture; they were about 97% pure. The sources of these materials are given in Table 3.

Table 3. Hugoniot elastic limits.

Material	Manufacturer	Density (g/cm^3)	Sample thickness (mm)	HEL (kbar)
B_4C	Norton Co., hot pressed	2.50	3.2	162 ± 9
			5.8	158 ± 4
			7.2	149 ± 20
			9.6	137 ± 4
BeO	Brush Beryllium Co., Thermalox 995	2.84	3.2	91 ± 11
			6.4	82 ± 10
			8.9	73 ± 10
			12.8	74
Al_2O_3	General Electric Co., Lucalox (Ref. 11)	3.97	6.4	112 ± 2
			12.7	111 ± 12
Al_2O_3	Carborundum Co., hot pressed	3.92	3.2	160 ± 6
			6.0	134 ± 5
			9.6	112 ± 3
			12.8	92 ± 3
Al_2O_3	Western Gold and Platinum Co. Al-955	3.81	6.4	83 ± 5
Al_2O_3	Diamonite P-3142-1	3.72	3.2	79 ± 5
			4.1	95 ± 2
			8.0	81 ± 4
			9.0	72
Al_2O_3	Coors Porcelain Co., AD-85	3.42	3.2	65
			6.3	61 ± 5
			9.6	61
SiC	Carborundum Co., Type KT	3.09	6.4	91 ± 15
TiB_2	Union Carbide	4.52	6.4	81 ± 35
AlB_{12}	LRL Powder from CERAC	2.54	6.4	32
$TiBe_{12}$	Brush Beryllium Co.	2.28	6.4	53
Be_2B	LRL Powder from CERAC	1.99	6.4	65
$ZrBe_{13}$ (2% Zr_2Be_{17})	Brush Beryllium Co.	2.73	6.4	71 ± 11
$\langle100\rangle$ Si	Ventron Electronics Corp.	2.330	6.4	92 ± 10
$\langle110\rangle$ Si	Ventron Electronics Corp.	2.330	6.4	53 ± 6
$\langle111\rangle$ Si	Ventron Electronics Corp.	2.330	6.4	54 ± 3
Vascomax 350	Vanadium Pacific Steel Co.	8.08	6.4	48

Vascomax 350 is a maraging steel; the composition is Fe, 11.8% Co, 18.1% Ni, 4.7% Mo, 1.36% Ti. It is manufactured by the Vanadium-Pacific Steel Company, Maywood, California.

Oriented single crystals of silicon were obtained from the Ventron Electronics Corporation, Bradford, Pennsylvania.

Theoretical and actual densities for the ceramics are listed in Table 2. Theoretical densities were calculated under the assumption that the impurities were all present as discrete crystals of the oxide. Probably some of the impurities formed silicates or aluminates, but this should not change the density much as long as the impurity is not present in large amounts. The AD-85 alumina ceramic was the most impure material studied, and the theoretical density of this material was calculated as 3.66 g/cc. (The density of crystalline

alumina is 3.986.) R. Landingham of LRL measured the density of crushed AD-85 with a helium picnometer. For a powder of grain size less than 37 μ, he measured a density of 3.635 ± 0.02 g/cc. Such a measurement is a lower limit on the theoretical density of the ceramic, whose bulk density is 3.42 g/cc, and this lends some confidence to the method used to calculate theoretical densities.

Longitudinal and shear sonic velocities were measured on each sample used in order to eliminate gross variations in properties between samples. These measurements, made by H. L. Dunegan and P. L. Knauss of LRL, were stated to be accurate within about 2%; sonic velocity scatter between samples was about ±2% from the average. Elastic moduli calculated from the average velocities obtained are listed in Table 2.

Results

Table 4. Axial yield strengths and phase-transition pressures.

Material	HEL (kbar)	Volume (cm^3/g)	First transition stress (kbar)	Volume (cm^3/g)	Second transition stress (kbar)	Volume (cm^3/g)
⟨100⟩ Si[a]	92 ± 10	0.406	None observed		140 ± 4	0.385
⟨110⟩ Si	53 ± 6	0.418	102 ± 6	0.399	131 ± 3	0.384
⟨111⟩ Si	54 ± 3	0.418	101 ± 3	0.400	137 ± 5	0.380
Vascomax 350[b]	48 ± 20	0.122	180 ± 3	0.115	—	—

[a]Initial volume = 0.429 cm^3/g.
[b]Initial volume = 0.134 cm^3/g.

Values of the stress at the HEL, the dynamic yield strength, and values of the stresses where phase transitions were seen are listed in Tables 2, 3, and 4.

Hugoniot Data for the entire series of experiments is summarized in Figs. 4 through 10, and fits to the Hugoniot data are given in Table 2.

-10-

If strain rates are negligible and equilibrium is achieved, the notion of a single-valued HEL is valid. In nonequilibrium cases, as exemplified by shock attenuation with propagation distance, it should be noted that the form of the driving pulse, which may be an artifact of the HE system and not square, may influence the value obtained for the HEL. In these cases the film trace of the free-surface cutoff may be rounded as shown in Fig. 11. Similar rounding may also be associated with dispersion as the elastic wave moves through the material. Where such rounding was observed, tan γ was taken from the initial slope of the rounded trace. This usually resulted in a larger value for tan γ and consequently a smaller free-surface velocity than would be obtained from the straight-line slopes associated with the square-wave pressure pulses. Despite the uncertainty caused by lack of equilibrium and nonsquare
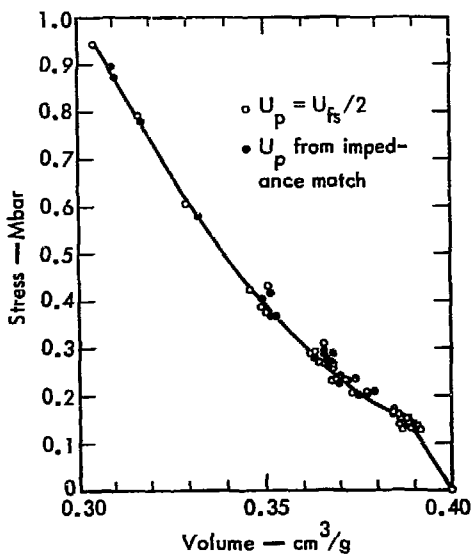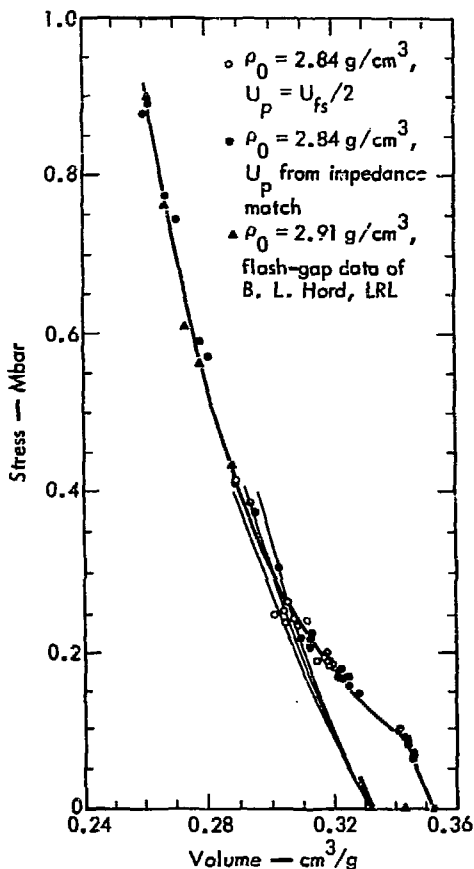
Fig. 5. Experimental Hugoniot for BeO ceramic. The light lines represent the range of uncertainty in the ultrasonically determined isotropic compression curve. The short heavy line is from the static compression work of Cline and Stephens (Ref. 4).

driving pulses, characteristic values for the HEL's have been assigned, but obviously these should be used with caution.

In the flash-gap measurements, U_s was less than C_L. This is consistent with earlier calculations[11] that indicated that the free-surface movement associated with the elastic wave was not sufficient to cause the gap to flash before the second wave
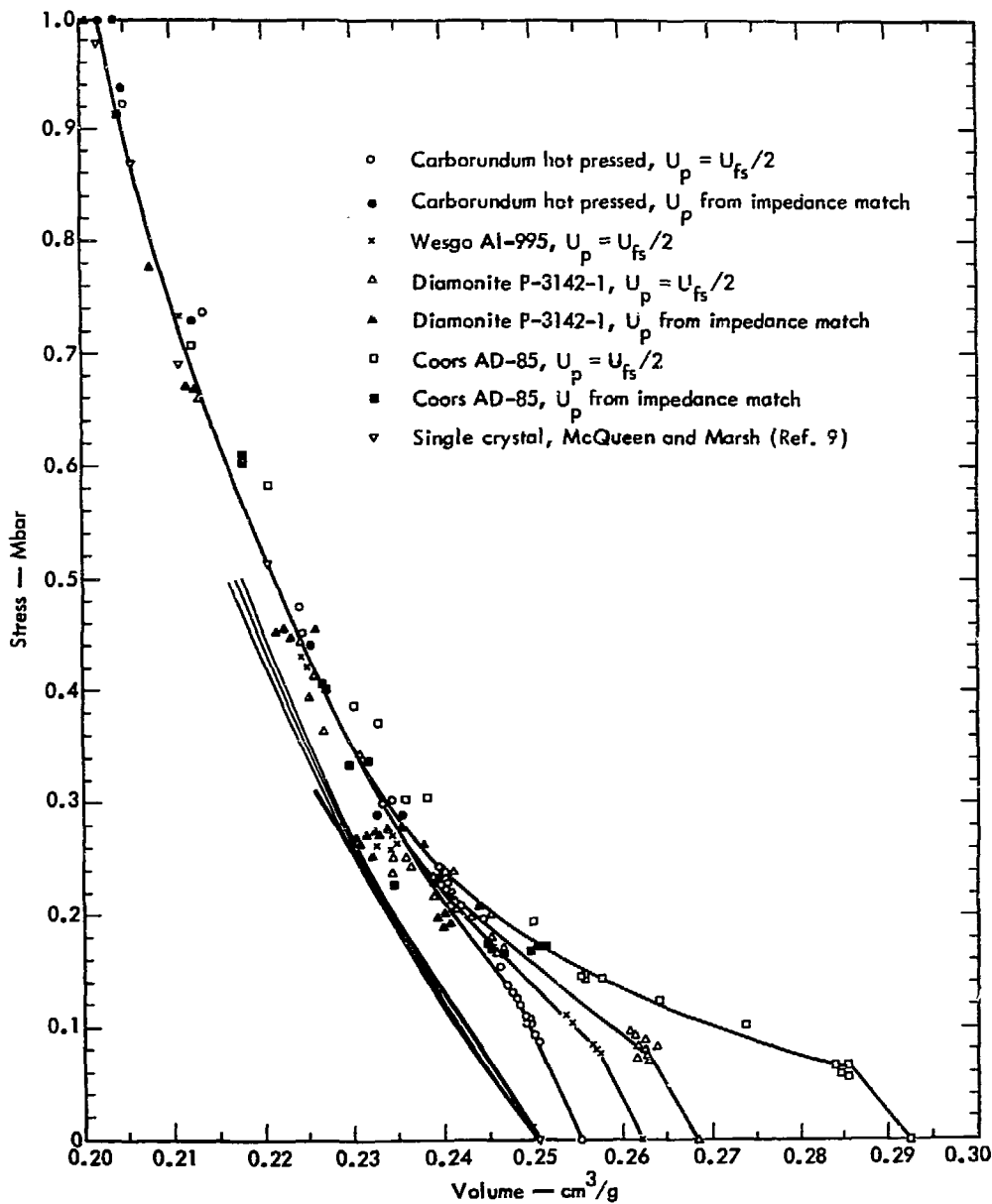
Fig. 4. Experimental Hugoniot for B_4C ceramic.

Fig. 6. Experimental Hugoniots for Al_2O_3 ceramics. The light lines represent the range of uncertainty in the ultrasonically determined isotropic compression curve. The heavy lines from the static compression work of Hart and Drickamer (Ref. 2).

arrived at the boundary. Hence, the re- corded flash-gap data are related to the second wave. In some instances where C_L was greater than U_s, the analysis was
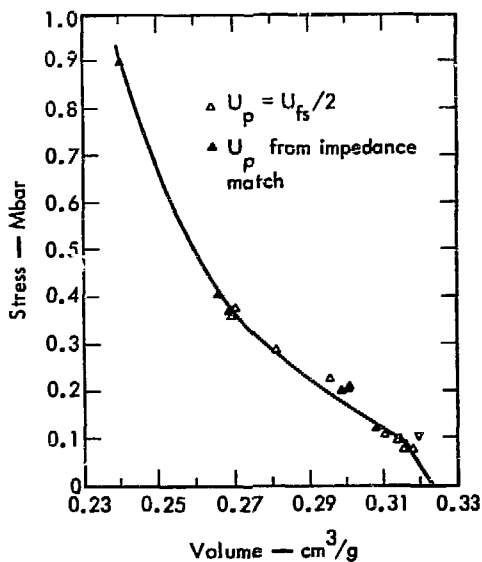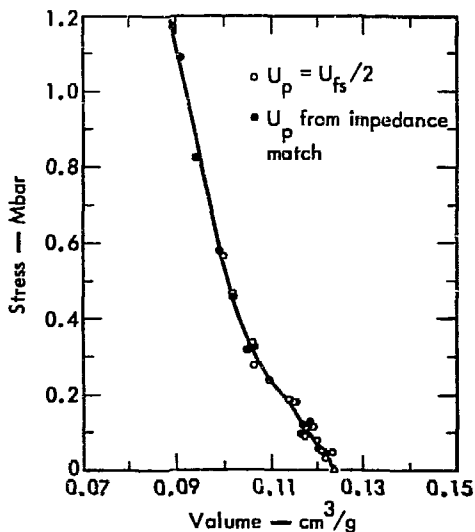
Fig. 7.   Experimental Hugoniot for SiC ceramic.
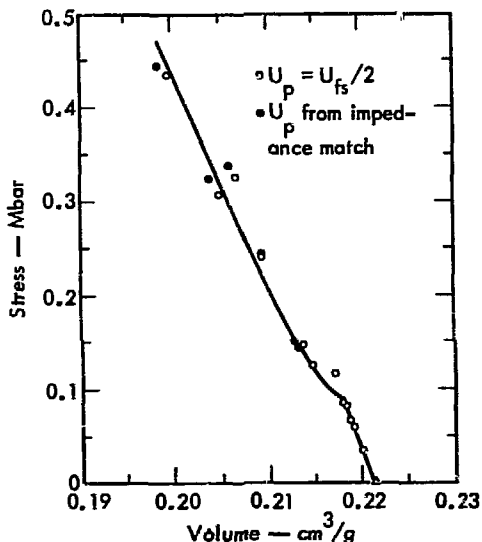

Fig. 9.   Experimental Hugoniot for Vascomax 350.

Fig. 8.   Experimental Hugoniot for TiB$_2$ ceramic.

made more exact by assuming average values for the elastic wave parameters and then applying two-wave data reduction

methods.   Where U_s is only slightly smaller than C_L, the two-wave treatment offered no improvement.

HEL's were obtained for all the materials studied.   In all cases multiple wave structures were observed, the leading wave propagating at near C_L.   The HEL's listed for B$_4$C are the highest recorded for any polycrystalline material.[24]   The HEL for Vascomax 350 is about twice as high as for any iron alloy previously measured.[24]   For the aluminas, the HEL's do not vary continuously with density.   Impurity content or material processing seems to be important.   Observation of the variation of HEL amplitude with sample thickness or shock propagation distance discloses possible precursor shock attenuation for B$_4$C and hot-pressed Al$_2$O$_3$.   However, variation in amplitude for given thicknesses was comparable to the apparent attenuation.   The other materials exhibited no consistent trend.   No major variation of
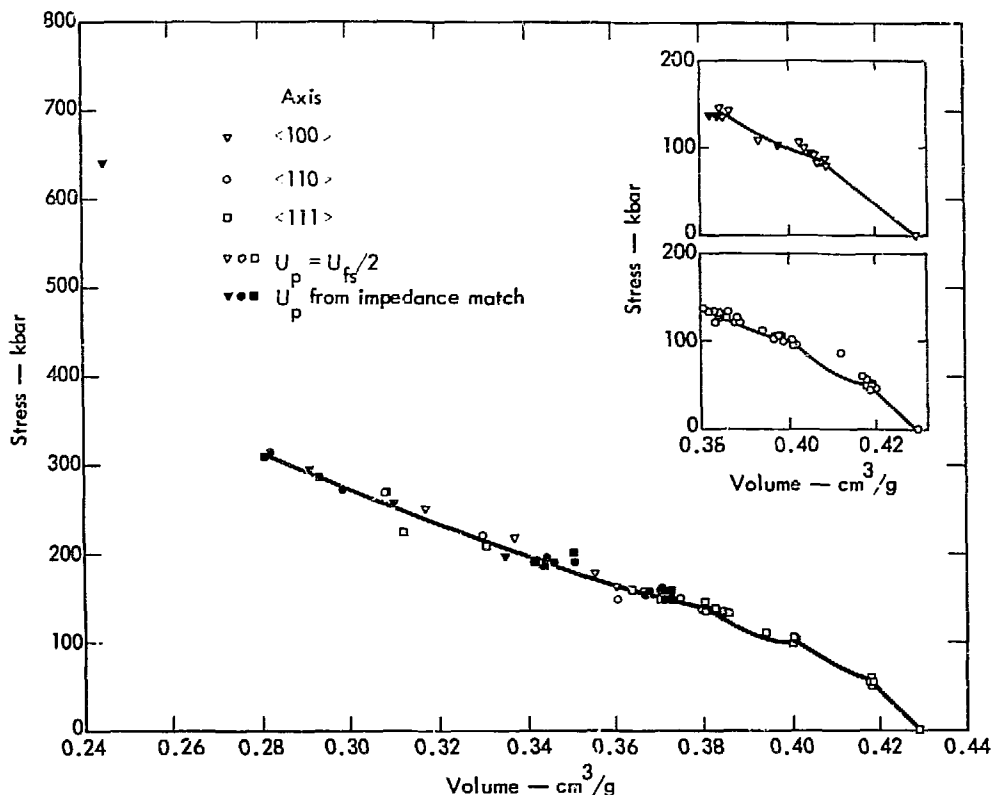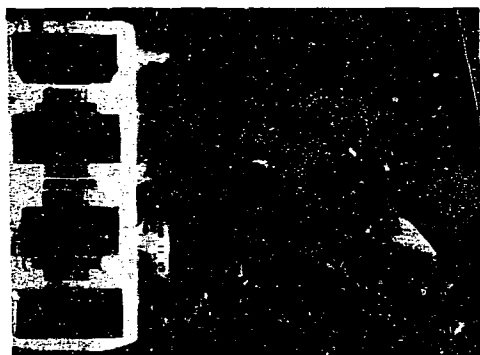
-13-

Fig. 10. Experimental Hugoniot for crystalline silicon.

Fig. 11. Streaking-camera film record from an inclined-mirror experiment on Diamonite Al$_2$O$_3$ P-3142-1, showing a curved film trace from a ramp-shaped wave, 200 kbar.

HEL amplitude with driving pressure was observed.

For the more porous materials, BeO and Diamonite and Coors Al$_2$O$_3$, it was noted that in the compaction regime, i.e., from the yield point to about 300 kbar, the value obtained for U$_{p_2}$ from impedance matching was consistently greater than U$_{fs_2}$/2. This is the opposite of results obtained for metals and is consistent with a model in which the porosity is permanently crushed out of the material by the shock compaction.

Figure 6 indicates that, within the limits of uncertainty involved, the four grades of Al$_2$O$_3$ converge to a Hugoniot which agrees

well with single crystal data obtained by McQueen and Marsh.[9]

In developing a representation of these Hugoniot results, as given in Table 2, a simple model was used. In this model, the crushing behavior of the porous materials is ignored, and the materials are assumed to behave according to an elastic, perfectly plastic model. In this case, one may obtain the pressure on compression by simply subtracting the quantity $\Delta\sigma$ from the measured longitudinal stress on compression, σ. Simple elasticity shows that

$$\Delta\sigma = 2Y_0/3 = (L - B)\sigma_{HEL}/L , \quad (9)$$

where Y_0 is the yield stress under uniaxial stress, σ_{HEL} is the stress at the Hugoniot elastic limit, and L and B are the longitudinal and bulk moduli, respectively.

The resulting P - V curve is then fitted with the polynomial

$$P = A_1\mu + A_2\mu^2 + A_3\mu^3 , \quad (10)$$

where

$$\mu = (V_0 - V)/V . \quad (11)$$

Since the temperature rise on the shock compression of these materials is small,[11] the omission of the energy term in the equation of state has no serious consequences, as long as it is used only for shock-wave problems. While this model provides an adequate description of the behavior of these materials under compression, it may not be adequate to describe their release behavior and should be used with caution.

The ceramics B_4C, BeO, and Al_2O_3 all have Hugoniots represented by a quadratic (P - μ) polynomial, i.e., $A_3 = 0$ in Eq. (10). For the more porous ceramics, A_1 is significantly less than the elastic bulk modulus, showing that the material is

crushing up in the pressure range of a few hundred kilobars. A large value for A_2 in these cases results from the curvature of the Hugoniot associated with the completion of crushing. At pressures below 500 kbar, the data scatter somewhat more than above, probably reflecting some nonrepeatability in the process of crushing up.

TiB_2 appears to behave in a similar way, except that the data do not extend to sufficiently high pressures to accurately determine the value of A_2. The data for SiC, on the other hand, are represented by a constant ratio P/μ ($A_2 = A_3 = 0$) below 400 kbar, but above that pressure the Hugoniot appears to stiffen markedly. The full range of the data is only roughly represented by the second fit given.

For AlB_{12}, $TiBe_{12}$, Be_2B, and $ZrBe_{13}$, only two shots were fired on each material. For this reason, the Hugoniot above the HEL can only be represented by a constant ratio P/μ. AlB_{12} exhibited a possible multiple wave structure, indicating a phase transition at 62 kbar (the quality of the record precludes a positive assignment). This transition is ignored in making the fit.

In crystalline silicon, two successive phase transitions were observed above the HEL. The pressures for these transitions varied with crystal orientation; they are given in Table 4. Surprisingly, the fit with $A_3 \neq 0$, which ignores the phase transitions, is a good representation of the data for all the orientations. The volume compression associated with the various transitions is taken up in the negative value of A_2.

The maraging steel Vascomax 350 shows a much larger effect of a phase transition

at 180 kbar. Accordingly, two fits are
given. Presumably the transition is the
bcc → hcp transition observed in pure iron
at 130 kbar.

Discussion

It has been noted[11,25] that the Hugoniots
for alumina and quartz are offset from the
isotropic or hydrostatic compression curve,
whereas for MgO, the Hugoniot and iso-
tropic compression curve are essentially
coincident. This offset has been interpreted
as the result of anisotropic stress in the
deformational state, since only the stress
component in the shock propagation direc-
tion is measured. Thus, a comparison of
the Hugoniot with an isotropic compression
curve will yield information on the stress
anisotropy behind the shock front.

The temperature rise on the shock
compression of the ceramics studied is
so small[11] that there is no need to dis-
tinguish between isothermal, isentropic,
and shock compression. Hence, sonic
measurements of the compressibility can
be used to produce an isotropic compres-
sion curve. We take this compression
curve in the Murnaghan form, which re-
quires the normal bulk modulus and its
pressure derivative as input parameters:[26]

$$P = \frac{B_{so}}{B'_{so}} \left[\left(\frac{V_0}{V}\right)^{B'_{so}} - 1 \right] \qquad (12)$$

This is, of course, based on the expansion
of the bulk modulus in a power series in
the pressure and the truncation of the series
after the linear term. Anderson[26] has
shown that this form is in agreement with
experimental data; the error introduced by
the truncation is less than the scatter in
his data. Yu,[27] on the other hand, has
attempted to evaluate the next term in the
series from Anderson's data.

Since we are going to extend the sonic
compression curve to 500 kbar, we must
have some estimate of the reliability of
the data and the equation-of-state form.
It may be noted that sonic measurements
have been reported by many authors,
particularly for Al_2O_3. Typically the
results reported by various authors differ
by amounts significantly greater than the
reported precision of the individual meas-
urements. Presumably this is due to
variations between the samples used by
different authors. For the purposes of this
work the various reported results have
been averaged, after some subjective at-
tempts to evaluate the individual reports.
The RMS deviations between reported
results were then taken as estimates of
the uncertainty in the averages. Data for
both single and polycrystalline samples
were used. The quadratic term in the
bulk modulus expansion was taken as zero,
and Yu's estimate of a 5% pressure con-
tribution at 500 kbar in Al_2O_3 was used to
estimate the error introduced by the omis-
sion of this term. These procedures may
be overly pessimistic, but it is difficult
to justify any smaller error limits.

Table 2 and Fig. 12 show the density
variation of the various moduli for the
slightly porous ceramic aluminas studied
in this work. Some of the sonic work re-
ported in the literature is also on materials
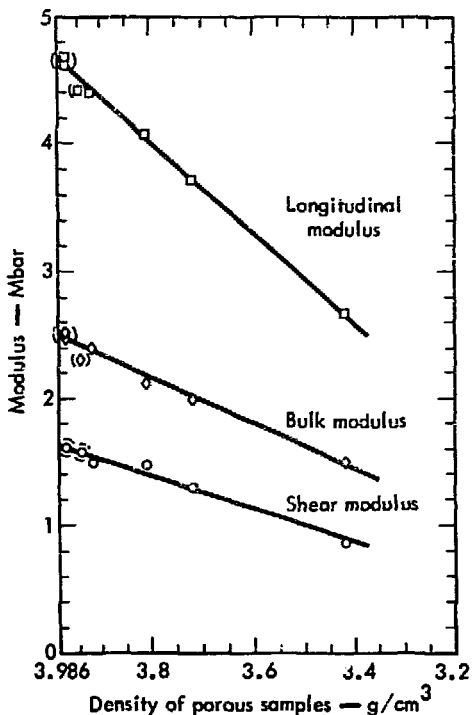of less than crystal density. These results

Fig. 12. Longitudinal, bulk and shear
moduli versus density for alu-
mina ceramics from ultrasonic
measurements.

taintes. The static compression meas-
urements of Hart and Drickamer[2] and
Cline and Stephens[4] are also shown.

With these isotropic compression
curves it is now possible to make some
determinations of the yield strengths of
the ceramic materials under compression.
For this purpose, it is convenient to define
a distention ratio α, similar to Herrmann's
α:[33,34]

$$\alpha(\sigma) = V_{Hug}(\sigma)/V_{iso}(\sigma) . \qquad (13)$$

Here $V_{Hug}(\sigma)$ and $V_{iso}(\sigma)$ are the specific
volumes on the Hugoniot and on the iso-
tropic compression curve at σ. The
volume for isotropic compression is taken
as the volume on the ultrasonic compres-
sion curve multiplied by the ratio of the
theoretical density given in Table 2 to the
theoretical density of the pure material.
Thus, the effect of impurities is assumed
only to result in a scaling of the density.
The compressibility is assumed for the
moment to be unaffected by impurities.

Figure 13 shows the values of α obtained
at the experimental Hugoniot points versus
longitudinal stress up to 500 kbar. Each
point on the figure is an average of all the
shots at that particular driving stress.

If the yield strength of the material is
nonzero under compression, the Hugoniot
will be offset from the isotropic compres-
sion curve by an amount $\Delta\sigma = (2/3)Y_0$,
where Y_0 is the yield strength under

were corrected to crystal density using the
slope from Fig. 12. Table 5 lists the
ultrasonic parameters resulting from this
analysis of the data in the literature, to-
gether with references to the original work.
Most important are the estimated accura-
cies for each parameter. The Murnaghan
isotropic compression curves are shown
in Figs. 5 and 6 together with the uncer-

Table 5. Ultrasonic bulk moduli for materials at theoretical density.

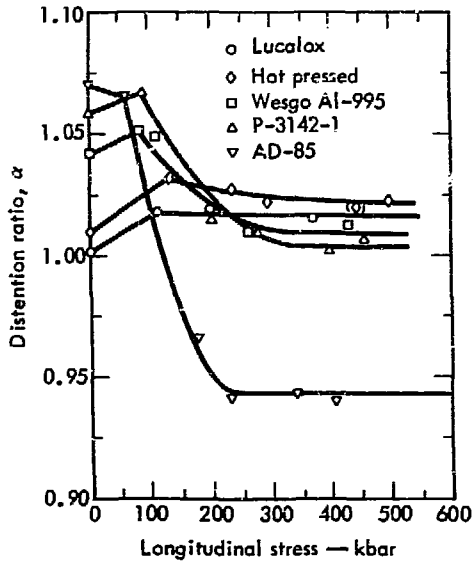| Material	ρ_0 (g/cm^3)	B_{so} (Mbar)	B'_{so} (Mbar)	References
Al$_2$O$_3$	3.986	2.51 ± 1%	4.2 ± 4%	5-7, 28-30, this work
BeO	3.01	2.25 ± 5%	5.5 ± 20%?	8, 30-32

Fig. 13. Distention ratio versus stress for alumina ceramics, $\alpha(\sigma) = V_{Hug}(\sigma)/V_{iso}(\sigma)$.

The data shown in Fig. 13 show this general behavior at pressures above the point where the compaction of the porosity of the materials is complete. However, for Diamonite 3142-1, α is not as much greater than 1 as for the other aluminas, and for Coors AD-85. α is actually less than 1 under compression, indicating a crossing of the isotropic compression curve and Hugoniot. The explanation of this anomaly is found in the presence of Si in these ceramics. Quartz undergoes a polymorphic transition to stishovite on compression.[20,22,35] This transition is accompanied by a 40% volume reduction. Other silicates exhibit similar transition.[36] Thus, the presence of the Si (or SiO_2) impurity in the Diamonite and Coors aluminas increases the compressibility of these ceramics, and our Al_2O_3 isotropic compression reference curve is not applicable. For the pure alumina ceramics, the limiting value of α is between 1.01 and 1.02, corresponding to values of $\Delta\alpha$ between 20 and 40 kbar. The exact values are given in Table 6, where the value of the stress offset corresponding to the HEL is also

uniaxial stress. This stress offset can be represented as a volume offset $\alpha - 1 = \Delta\sigma/B$, where B is the bulk modulus. Thus, above the yield point, α should be greater than 1 and roughly constant for a nonporous material with a constant yield strength.

Table 6. Distention ratios and stress offsets in BeO and Al_2O_3.

	BeO	Al_2O_3 AD-85	Al_2O_3 P-3142-1	Al_2O_3 Al-995	Al_2O_3 Hot pressed	Al_2O_3 Lucalox
Density, ρ_0 (g cm³)	2.84 ± 0.01	3.42 ± 0.02	3.72 ± 0.02	3.81 ± 0.02	3.92 ± 0.01	3.97 ± 0.01
Theo density (g cm³)	3.01 ± 0.01	3.66 ± 0.05	3.94 ± 0.01	3.97 ± 0.01	3.96 ± 0.01	3.98 ± 0.01
Void fraction ($= 1 - \rho/\rho_{th}$)	0.056 ± 0.005	0.065 ± 0.02	0.055 ± 0.007	0.040 ± 0.007	0.008 ± 0.003	0.002 ± 0.003/0.002
HEL (6mm) (kbar)	82 ± 10[a]	61 ± 5	88 ± 5	88 ± 5	134 ± 8[a]	112 ± 12
α(high pressure)	(0.997 ± 0.015)[b]	(0.943 ± 0.02)[c]	(1.004 ± 0.005)[c]	1.010 ± 0.003	1.022 ± 0.005/0.035	1.017 ± 0.003
α_{HEL}	1.072 ± 0.005[b]	1.066 ± 0.02[c]	1.067 ± 0.01[c]	1.051 ± 0.01	1.032 ± 0.003	1.018 ± 0.002
α_0	1.70 ± 0.005	1.070 ± 0.02[c]	1.059 ± 0.007	1.042 ± 0.007	1.010 ± 0.003	1.002 ± 0.002
$\Delta\alpha = \alpha_{HEL} - \alpha_0$	0.012 ± 0.001[b]	-0.004 ± 0.001[c]	0.000 ± 0.001	0.009 ± 0.001	0.022 ± 0.001	0.015 ± 0.001
$\delta_0 = \alpha_{HEL} - \alpha_{HP}$	1.075 ± 0.015[b]	0.133 ± 0.02[c]	0.063 ± 0.005[c]	0.041 ± 0.003	0.010 ± 0.003/0.005	0.001 ± 0.002
$\Delta\alpha = \frac{2}{3}Y_0 \left(\frac{L-B}{L}\right) = _{HEL}$	41 ± 5[a]	27 ± 3	41 ± 3	40 ± 3	62 ± 4	52 ± 5
$\Delta\sigma = (\alpha_{HP} - 1)B$	—[b]	—[c]	—[c]	20 ± 6	53 ± 12	43 ± 8

[a]HEL is thickness-dependent; thick samples yield lower values.

[b]Large uncertainties result from poorly defined ultrasonic reference curve.

[c]Material containing appreciable Si compared against reference curve for pure Al_2O_3 corrected for theoretical initial density.

-18-

tabulated. The latter was calculated as $(L - B)\sigma_{HEL}/L$, where L is the longitudinal modulus and B the bulk modulus from Table 2. The stress offset from the high-pressure value of σ is given by $(\alpha_{HP} - 1)B$. It is interesting that for Al_2O_3, the yield strength above the HEL decreases some-what from its value at the HEL, but that it is always a least half of the HEL value.

For BeO, on the other hand, the Hugoniot appears to collapse to the iso-tropic compression curve above the HEL, thus indicating a major loss of strength on yielding.

The compaction behavior of porous materials has been of considerable inter-est in recent years.[33,34,37-39] The work most relevant for comparison with this work on ceramics is that on sintered porous metals.[34,39] For these materials, a quadratic variation of α with stress or pressure has been used in the compaction region.[33,34] Let σ_a and α_a ($=\alpha_{HP}$) rep-resent the stress and value of α at the point where compaction is complete, and σ_{HEL} and α_{HEL} the values at the HEL. (In Table 6, α_0 is the value for the un-compressed material.) We can write

$$\alpha(P) = \alpha_a + \frac{(\alpha_{HEL} - \alpha_a)(\sigma_a - \sigma)^2}{(\sigma_a - \sigma_{HEL})^2}. \quad (14)$$

Values of σ_a for the aluminas were esti-mated from an inspection of Fig. 13 and are close to $4\sigma_{HEL}$. The curves drawn in Fig. 13 are actually this quadratic expres-sion, and the agreement with the experi-mental data appears to be quite satisfactory.

Four-wave shock structures, as evi-denced by four discrete straight-line slopes on the photographic record, were found in experiments in which the shocks were propagated along the $\langle 110 \rangle$ and $\langle 111 \rangle$ axes of crystalline silicon. Close agreement between U_{S_1} and C_L, the ultrasonically determined longitudinal sound speed at 1 bar, indicated that the first wave was elastic. The possibility of the second wave also being elastic was excluded, since for cubic symmetry the principal propagation directions allowing pure mode propagation are the $\langle 100 \rangle$, $\langle 110 \rangle$, and $\langle 111 \rangle$ axes. The second and third waves were therefore taken to be related to two succeeding phase transitions.

In some experiments, the fourth wave was not observed because the observation time allowed by the prism angle of in-clination was not long enough. In others, the first phase transition was overdriven so that only three components were seen.

Shocks propagated along the $\langle 100 \rangle$ axis showed only three resolvable components: the first was the elastic wave, and the second a phase transition wave which occured at nearly the same (P, V) point as the second phase transition wave for samples of the $\langle 110 \rangle$ and $\langle 111 \rangle$ orientation. It was noted that in the region of the film record where one might expect a discon-tinuity related to the first phase transition the record was very fuzzy, thus indicating the possibility of two competing waves with nearly equal shock velocities.

In the $\langle 100 \rangle$ direction, the HEL appeared to increase from about 82 to 107 kbar as driving pressure varied from 100 to 360 kbar. This scatter may well be related to mixing between the HEL and an unresolved phase transition which should correspond to the 102-kbar transition found for the $\langle 110 \rangle$ and $\langle 111 \rangle$ axes. If this is assumed, the data could be divided so that the HEL would be about 85 kbar, with

a phase transition at about 100 kbar. Experiments with thicker samples to allow greater transit-time differences might allow resolution of the two waves.

Summary

1. Two-wave structures in several ceramics are interpreted as resulting from elastic and deformational compression. The Hugoniot elastic limit (HEL), taken as the amplitude of the first wave, then provides a measure of the yield strength of the ceramic.

2. At higher pressures, the yield strength is estimated from the pressure or volume offset between the Hugoniot and isotropic compression curve, the latter being estimated from ultrasonic data. For Al_2O_3 this yield strength is comparable to but somewhat smaller than the yield strength at the HEL. For BeO the comparison is less clear, but it appears that BeO probably loses most of its strength above the HEL. The behavior of Al_2O_3 is similar to that of quartz, whereas the behavior of BeO appears to be similar to MgO.

3. In the regime of partial compaction, a quadratic variation of distention with pressure appears to apply. Material released from such states appears to return to a higher density than its initial density.

Acknowledgments

References

1. P. W. Bridgman, Proc. Am. Acad. Arts Sci. 77, 187 (1949).
2. M. V. Hart and H. G. Drickamer, J. Chem. Phys. 43, 2265 (1965).
3. C. E. Weir and L. Shastis, J. Am. Ceram. Soc. 39, 319 (1956).
4. C. F. Cline and D. R. Stephens, J. Appl. Phys. 36, 2869 (1965).
5. E. Schreiber and O. L. Anderson, J. Am. Ceram. Soc. 49, 184 (1966).
6. D. H. Chung and G. Simmons, J. Appl. Phys. 39, 5316 (1968), and references therein.
7. J. H. Gieske and G. R. Barsh, Phys. Stat. Sol. 29, 121 (1968).
8. N. Soga, J. Am. Ceram. Soc. 51, 246 (1968) and references therein.
9. R. G. McQueen and S. P. Marsh, Ch. 7 of Handbook of Physical Constants, Revised Edition, S. P. Clark, Jr., Ed. (Geological Society of America, New York, 1966).
10. W. P. Brook and R. A. Graham, Bull. Am. Phys. Soc. 11, 414 (1966).
11. T. J. Ahrens, W. H. Gust, and E. B. Royce, J. Appl. Phys. 39, 4610 (1968).
12. S. Minomura and H. G. Drickamer, J. Phys. Chem. Solids 23, 451 (1962).
13. R. H. Wentorf, Jr. and J. S. Kasper, Science 139, 338 (1963).
14. J. C. Jamieson, Science 139, 764 (1963).
15. R. G. McQueen, in Metallurgy at High Pressures and High Temperatures (Gordon and Breach, New York, 1964), p. 80.
16. L. V. Al'tshuler, Soviet Phys. Usp. 8, 82 (1965).
17. M. N. Pavlovskii, Soviet Phys. Solid State, 9, 2514 (1968).
18. Preliminary reports of this work were presented at the meetings of the A.P.S. at Los Alamos, 1968, and Hawaii, 1969. W. H. Gust and E. B. Royce, Bull. Am. Phys. Soc. 13, 901 (1968); W. H. Gust and E. B. Royce, Bull. Am. Phys. Soc. 14, 833 (1969).
19. J. M. Walsh and R. H. Christian, Phys. Rev. 97, 1544 (1955).
20. G. R. Fowles, J. Geoph. Res. 72, 5729 (1967); Stanford Research Institute Report, PLTR 003-61 (1961); D. G. Doran, J. Appl. Phys. 34, 844 (1963).
21. G. Eden and P. W. Wright, in Fourth Symposium on Detonation, ACR-126-ONR (Washington, D. C., 1965), p. 573.
22. Jerry Wackerle, J. Appl. Phys. 33, 922 (1962).
23. A. Taylor, B. J. Kagle, Crystallographic Data on Metal and Alloy Structures (Dover, 1963).
24. O. E. Jones and R. A. Graham, Paper presented at NBS Symposium on Accurate Characterization of the High-Pressure State (1968), to be published; Sandia Laboratories Report SC-R-68-1857 (1968).
25. T. J. Ahrens and R. K. Linde, in Behavior of Dense Media at High Dynamic Pressures (Gordon and Breach, New York, 1968), p. 325.

26. O. L. Anderson, J. Phys. Chem. Solids 27, 547 (1966); Phys. Earth Planet. Interiors 1, 169 (1968).

27. J. S. Yu, Appl. Sci. Res. 19, 220 (1968).

28. N. Soga and O. L. Anderson, J. Am. Ceram. Soc. 49, 355 (1966).

29. D. H. Chung and W. R. Bussem, J. Appl. Phys. 39, 2777 (1968), and references therein.

30. O. L. Anderson, E. Schreiber, and R. C. Lieberman, Rev. Geoph. 6, 491 (1968), and references therein.

31. C. F. Cline, H. L. Dunegan, and G. W. Henderson, J. Appl. Phys. 38, 1944 (1967).

32. G. G. Bentle, J. Am. Ceram. Soc. 49, 125 (1966).

33. W. Herrmann, J. Appl. Phys. 40, 2490 (1969); Sandia Laboratories Reports SC-DR-68-321 (1968); SC-RR-66-2678 (1967).

34. B. M. Butcher and C. H. Karns, J. Appl. Phys. 40, 2967 (1969); Sandia Laboratories Report SC-RR-67-3040 (1968).

35. R. G. McQueen, J. N. Fritz, and S. P. Marsh, J. Geoph. Res. 68, 2319 (1963).

36. R. G. McQueen, S. P. Marsh, and J. N. Fritz, J. Geoph. Res. 72, 4999 (1967).

37. R. K. Linde and D. N. Schmidt, J. Appl. Phys. 37, 3259 (1966).

38. P. C. Lysne and W. J. Halpin, J. Appl. Phys. 39, 5488 (1968).

39. R. R. Boade, J. Appl. Phys. 39, 5693 (1968); 40, 3781 (1969).